Increasing risk of another Cape Town "Day Zero" drought in the 21st century

Salvatore Pascale[a,b,c,1], Sarah B. Kapnick[b], Thomas L. Delworth[b], and William F. Cooke[b]

[a]Department of Earth System Science, Stanford University, Stanford, CA 94305; [b]Geophysical Fluid Dynamics Laboratory, National Oceanic and Atmospheric Administration, Princeton, NJ 08540; and [c]Atmospheric and Ocean Sciences Program, Princeton University, Princeton, NJ 08544

Edited by Dennis L. Hartmann, University of Washington, Seattle, WA, and approved September 28, 2020 (received for review May 7, 2020)

Three consecutive dry winters (2015–2017) in southwestern South Africa (SSA) resulted in the Cape Town "Day Zero" drought in early 2018. The contribution of anthropogenic global warming to this prolonged rainfall deficit has previously been evaluated through observations and climate models. However, model adequacy and insufficient horizontal resolution make it difficult to precisely quantify the changing likelihood of extreme droughts, given the small regional scale. Here, we use a high-resolution large ensemble to estimate the contribution of anthropogenic climate change to the probability of occurrence of multiyear SSA rainfall deficits in past and future decades. We find that anthropogenic climate change increased the likelihood of the 2015–2017 rainfall deficit by a factor of five to six. The probability of such an event will increase from 0.7 to 25% by the year 2100 under an intermediate-emission scenario (Shared Socioeconomic Pathway 2-4.5 [SSP2-4.5]) and to 80% under a high-emission scenario (SSP5-8.5). These results highlight the strong sensitivity of the drought risk in SSA to future anthropogenic emissions.

drought | climate-change detection | climate extremes | event attribution | large ensemble simulations

The Day Zero Cape Town drought was one of the worst water crises ever experienced in a metropolitan area (1, 2). Droughts are a regular occurrence in southwestern South Africa (SSA), having occurred during the late 1920s, early 1970s, and, more recently, during 2003–2004 (Fig. 1 *A* and *B*). However, the extended winter (April to September [AMJJAS]) 3-y rainfall deficit (Fig. 1 *A* and *B*; *SI Appendix*, Fig. S1) which drove the 2015–2017 Cape Town drought (2–8) was exceptional over the last century (4, 9). Storage in reservoirs supplying water to 3.7 million people in the Cape Town metropolitan area dropped to about 20% of capacity in May 2018. As a consequence, strict water-usage restrictions were implemented to delay water levels reaching 13.5%, the level at which much of the city's municipal supply would have been disconnected (7), a scenario referred to as "Day Zero" by the municipal water authorities (7). Above-average winter rain over the rest of the 2018 austral winter allowed Cape Town to avoid the Day Zero scenario.

While poor water-management practices and infrastructure deficiencies worsened the crisis (10, 11), the 2015–2017 rainfall deficit was the main driver of the drought (5). To facilitate the improvement of water-management practices and the infrastructure necessary to make the system more resilient, it is critical to first determine how likely a meteorological drought like the one in 2015–2017 might be in the coming decades. Increased aridity is expected in most of southern Africa (12–14) as a consequence of the Hadley Cell poleward expansion (4, 15–18) and southward shift of the Southern Hemisphere jet stream (19). Second, the risk of more extreme droughts should be quantified to understand the potential for emerging risks that could make a Day Zero event in Cape Town unavoidable.

Previous work (5) has suggested that the Day Zero drought may have been made 1.4 to 6.4 times more likely over the last century due to +1 K of global warming, with the risk expected to scale linearly with one additional degree of warming. Such estimates make use of statistical models of the probability distribution's tail (e.g., the generalized extreme value) applied to observations and previous-generation [i.e., as those participating to the Coupled Model Intercomparison Project Phase 3 (CMIP3) (20) and 5 (21)] climate models. CMIP3 and CMIP5 models have been shown to have a systematically biased position of the Southern Hemisphere jet stream toward the Equator, due to insufficient horizontal resolution (19). This produces a large uncertainty in model projections of jet-stream shifts (22, 23), thus hindering realistic projections of Southern Hemisphere climate change. Furthermore, for hydroclimatic variables, a statistical extrapolation of the probability distribution's tail might have inherent limitations in providing precise estimates of the event probability of future extreme events, although its precision profits from the use of large ensembles (24, 25).

Large ensembles of comprehensive climate models provide thousands of years of data that allow direct construction of the underlying probability distribution of hydroclimatic extremes without relying on a hypothesized statistical model of extremes (25, 26). South African winter rains have high interannual and decadal variability due to El Niño–Southern Oscillation (27), the Southern Annular Mode (28), and interdecadal variability (29). A multidecade to multicentury record may be required to detect the emergence of statistically significant trends in regional precipitation extremes. A large ensemble is, thus, a powerful method to isolate, at the decadal timescale, internal natural variability (e.g., *SI Appendix*, Fig. S2) from the forced signal (30–32).

Significance

The Cape Town "Day Zero" drought was caused by an exceptional 3-y rainfall deficit. Through the use of a higher-resolution climate model, our analysis further constrains previous work showing that anthropogenic climate change made this event five to six times more likely relative to the early 20th century. Furthermore, we provide a clear and well-supported mechanism for the increase in drought risk in SSA through a dedicated analysis of the circulation response, which highlights how—as in 2015–2017—a reduction in precipitation during the shoulder seasons is likely to be the cause of drought risk in southwestern South Africa in the 21st century. Overall, this study greatly increases our confidence in the projections of a drying SSA.

Author contributions: S.P. designed research; S.P. performed research; S.P. analyzed data; S.P. wrote the paper; S.B.K. and T.L.D. took part in the discussion of the results; S.B.K., T.L.D., and W.F.C. contributed to the writing; T.L.D. designed the ensemble; and W.F.C. performed the numerical simulations.

The authors declare no competing interest.

This article is a PNAS Direct Submission.

[1]To whom correspondence may be addressed. Email: pascaledeep@gmail.com.

This article contains supporting information online at https://www.pnas.org/lookup/suppl/doi:10.1073/pnas.2009144117/-/DCSupplemental.

First published November 9, 2020.

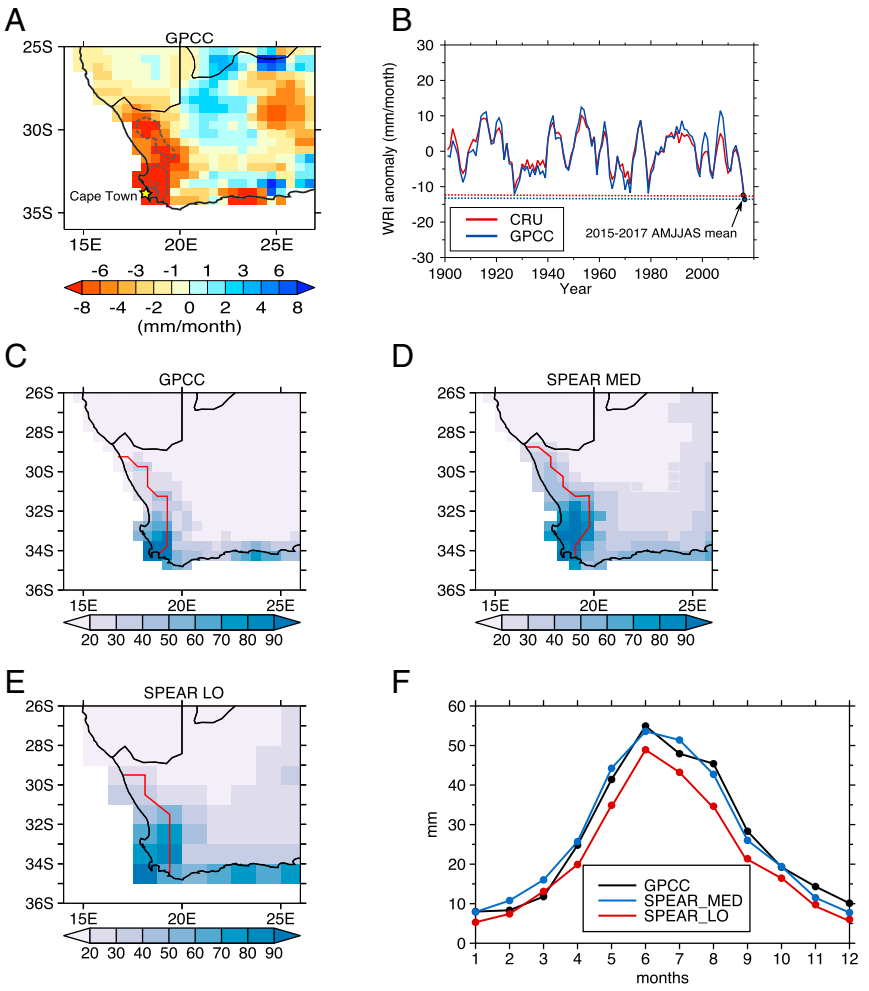

Fig. 1. (*A*) Mean 2015–2017 AMJJAS rainfall anomaly relative to 1921–1970. The dashed (continuous) line denotes negative anomalies beyond 1 (1.5) SD. (*B*) Time series of the observed (GPCC, blue; CRU, red) 3-y running mean AMJJAS WRI (*Materials and Methods*) from 1901 to 2017. The 2015–2017 mean is record-breaking over the period 1901–2017. (*C*–*E*) Mean 1921–1970 AMJJAS rainfall (millimeters per month) in observations (GPCC) (*C*), SPEAR_MED (*D*), and SPEAR_LO (*E*). The red lines encircle the area receiving at least 65% of the total annual rainfall during AMJJAS used to define WRI. (*F*) Monthly WRI in observations and models. Comparison of SPEAR_MED with SPEAR_LO shows how an enhanced resolution is key to capture finer-scale regional details of winter rainfall in the relatively small SSA Mediterranean region.

The Seamless System for Prediction and Earth System Research Large Ensemble

To tackle this problem, we used a comprehensive suite of large-ensemble simulations from the newly developed Seamless System for Prediction and Earth System Research (SPEAR) global climate model developed (33) at the Geophysical Fluid Dynamics Laboratory (GFDL; *Materials and Methods*). SPEAR is the latest GFDL modeling system for seasonal to multidecadal prediction and projection, and it shares underlying component models with the CM4 (34) climate model, which participates to the Coupled Model Intercomparison Project Phase 6 (CMIP6) (35). In particular, we use the medium horizontal atmospheric resolution (50 km) version of SPEAR—i.e., SPEAR_MED, which has been designed to study regional climate and extremes. The SPEAR_MED simulations include a 3,000-y preindustrial control simulation (CTRL) and three 30-member ensembles that account for changing atmospheric compositions arising from natural sources only (NATURAL) and natural plus anthropogenic sources (HIST + Shared Socioeconomic Pathway 2-4.5 [SSP2-4.5] and HIST + SSP5-8.5; see *Materials and Methods* for details). The relatively high horizontal resolution of SPEAR_MED—which makes this large ensemble unique—is key to better resolving the steep coastal SSA topography, which leads to orographic enhancement of rainfall during frontal days (4). SPEAR_MED is an excellent tool to investigate SSA droughts because it has a realistic representation of the SSA winter rainfall pattern (Fig. 1 *C* and *D*) and seasonal cycle (Fig. 1*F*), and it correctly reproduces the amplitude of the interannual, multiannual, and decadal natural variability of the SSA winter rainfall (*SI Appendix*, Fig. S3).

Event Attribution to Anthropogenic Climate Change

As anthropogenic global warming weakens the basic stationarity assumption which has historically been at the foundation of water management (36), two key questions are: To what extent did anthropogenic global warming make the Day Zero drought more likely? And, how will the probability of occurrence of another similar or worse meteorological drought change in the coming decades? To address these questions, we first assess if the probability distribution of anomalies of the 3-y-mean Winter Rainfall Index (WRI; *Materials and Methods*) has already significantly changed. We directly compare the time-evolving probability distribution associated with successive 20-y time windows with that associated with only internal climate

variability obtained from a long control run at preindustrial forcing (CTRL; see *Materials and Methods* for details). The two probability distributions are statistically indistinguishable at the 99.9% level per the Kolmogorov–Smirnov test, during the 20-y period 1980–2000 (Fig. 2*A*), but then start to significantly differ from 1990–2010 onward (Fig. 2 *B*–*D*). Hereafter, we refer to the 2015–2017 WRI negative anomaly as "event_1517." The average of the event_1517 probabilities in the five decades 1921–1970 is ∼0.7% (Fig. 2*E*). This is slightly smaller than the value from the 3,000-y preindustrial control run and with the NATURAL experiment (1%)—which profit from the much longer time span (*SI Appendix*, Fig. S4*A*)—but, nevertheless, consistent within the 95% uncertainty interval. The event probability is stationary up to 1980–2000, after which it starts increasing (Fig. 2*E*). For 2015–2017, the event probability—obtained by linear interpolation of the 2000–2020 and 2010–2030 values—is 3.7% with a [2.5%,4.7%] 95% CI. This implies a risk ratio—i.e., the ratio of the probability of the event at given time to its probability in the early 20th century—of 5.5 times, with a CI of four to eight (Fig. 2*G*). Thus, an extreme event that had an average recurrence interval (37) of 100 years in the early 20th century reduces to a 25-y recurrence interval by present day. This is consistent with previous work (5), despite the different event definition between the two studies.

Drought Risk Projections

In the high-emission scenario SSP5-8.5 (intermediate-emission scenario SSP2-4.5), the event_1517 probability—i.e., the likelihood that rainfall is below the event_1517 threshold for any random 3-y segment within the 20-y window—is projected to rise to 20% (13%) around 2045 (Fig 2*F* and *SI Appendix*, Figs. S5 and S6) and to reach 80% (25%) by the end of this century. For the SSP5-8.5 (SSP2-4.5) scenario, the likelihood of an event_1517 would thus increase by a factor of 120 (40) relative to earlier in the 20th century (Fig. 2*H*). Extending the findings of previous studies (5) beyond +2 K of mean global surface temperature increase, we find that, for each degree of warming, the risk ratio grows at a slower rate after a fast, ongoing acceleration (*SI Appendix*, Fig. S7). This implies a transition to substantially drier and persistent wintertime conditions over SSA.

Using the same methodology (*Materials and Methods*), we can also estimate the distribution and the probability of occurrence of a 4-y WRI anomaly at the same intensity of event_1517 (Fig. 2 *I* and *J*). This has not occurred yet, but, if it occurred, could lead to an unavoidable Day Zero. In the absence of anthropogenic forcing (i.e., CTRL and NATURAL), such an event has a probability of occurrence of 0.4% (vs. ∼1% for a 3-y drought). Presently, the probability of occurrence for it to happen has already substantially increased relative to the early 20th century (2%), and it is projected to be 15% (8%) by midcentury under SSP5-8.5 (SSP2-4.5). By the end of the 21st century, a 4-y WRI anomaly will be almost as likely as 3-y rainfall anomaly of intensity comparable to the 2015–2017 event.

This suggests that the duration of meteorological droughts will increase in SSA. We estimate the probability distribution of the severe (i.e., ≤ -6 mm·month^{-1}) winter (i.e., AMJJAS) WRI anomalies as a function of duration and intensity under the SSP2-4.5 (Fig. 3 *A*–*C*) and SSP5-8.5 scenarios (Fig. 3 *D*–*F*). Historically, the largest (in magnitude) negative WRI anomalies typically last 1 y. There is a nonnegligible probability of 2- to 3-y persisting anomalies at about -10 mm·month^{-1}, while anomalies lasting longer than 3 y are unlikely (Fig. 3). Anthropogenic climate change will make meteorological winter droughts lasting 3 to 10 y more likely and more acute, especially under the SSP5-8.5 scenario (Fig. 3 *D*–*F*).

Large-Scale Circulation Shifts

The future increase in the probability of occurrence of intense and prolonged rainfall deficits (Figs. 2*F* and 3) is suggestive of a substantial climatic shift in the mean wintertime conditions of SSA in the coming decades. In agreement with state-of-the-art general circulation models (6, 38), SPEAR_MED indicates a substantial AMJJAS WRI reduction during the 21st century (*SI Appendix*, Fig. S8*A*), especially in the shoulder seasons of April–May (AM) and August–October (*SI Appendix*, Fig. S8*B*). In both scenarios, the amplitude of the shift will be outside the range of what could occur from low-frequency internal climate variability in the decade 2020–2030 (Fig. 4 *A*–*C*), but the magnitude of the negative anomaly will be substantially larger under a high-emission scenario.

The prolonged rainfall deficit experienced during winters 2015–2017 occurred along with positive large-scale anomalies in sea-level pressure on the southern flank of the South Atlantic and South Indian Subtropical High (3, 4). Higher sea-level pressure has been invoked as the cause of fewer extratropical cyclones over the South Atlantic and of a southward shift of the moisture corridors, contributing to winter rainfall (3). Other studies (4) find no significant regional trends over the last 40 y in the number of cold fronts making landfall over SSA, but highlight the shorter duration of rainfall events associated with cold fronts due to larger sea-level pressure during postfrontal days. Positive significant trends in sea-level pressure have been observed in the Southern Hemisphere over the last 40 y and have been related to the multidecadal expansion of the Southern Hemisphere's summer and fall Hadley Cell (15, 16, 18). In SPEAR_MED, the forced (i.e., ensemble mean) decadal changes in sea-level pressure are visible in the period 1980–2020 (*SI Appendix*, Fig. S9), with the typical patterns that might dominate at the end of the 21st century (*SI Appendix*, Fig. S10) emerging around 2000–2010. This is in agreement with previous studies (16, 17), suggesting that the forced signal associated with the expansion of the Hadley Cell has emerged above the noise of internal variability in the Southern Hemisphere in the 2000–2010 decade.

There is an evident seasonality in the projected large-scale circulation anomalies over the South Atlantic Ocean and south of SSA, with the most evident forced signals in AM and August–September (AS) (Fig. 5). Positive anomalies of mean sea-level pressure are overall suggestive of a poleward expansion of the Hadley cell. Projected changes in the 300-hPa eddy kinetic energy (a proxy for the storm track) show a southward shift of the midlatitude storm track in AM and AS, but not June–July (JJ). Indeed, the weakest forced signals are projected in SPEAR_MED at the peak of the rainy season in JJ (Fig. 5), consistent with the decadal forced mean sea-level pressure signals in the 2010–20 decade (*SI Appendix*, Fig. S9) and with the percent WRI reductions (*SI Appendix*, Fig. S8*B*). Remarkably, the 2015–2017 meteorological drought was also driven mainly by AM and AS rainfall deficits, associated with large-scale anomalies more evident in, e.g., AM, and similar to those just described above (3, 4, 6). These seasonal aspects of the Southern Hemisphere forced circulation changes coherently suggest that future meteorological droughts might indeed have a similar seasonal evolution as that in 2015–2017.

Comparison with Other Large Ensembles

We analyzed additional large ensembles from coupled models with the same or coarser resolution that can provide an important context to our results and inform us about uncertainties due to model differences (32, 39): SPEAR_LO; the Forecast-Oriented Low Ocean Resolution model with (FLOR_FA) and without (FLOR) flux adjustment; the Community EARTH

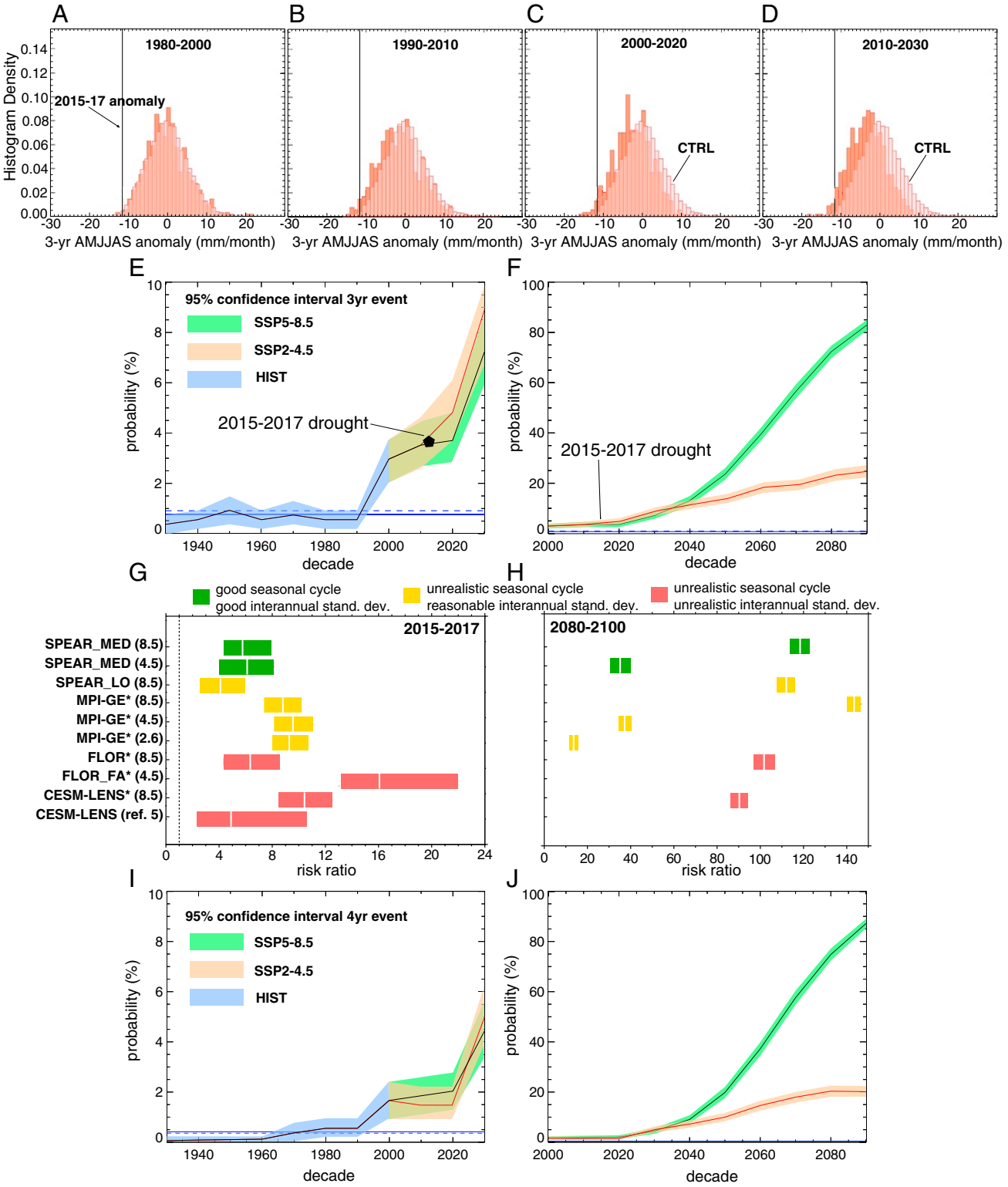

Fig. 2. (*A*–*D*) Empirical probability distribution of the 3-y winter rainfall anomalies due to internal variability alone (light pink, from CTRL) and natural variability, natural forcing, and anthropogenic forcing (salmon, from SSP5-8.5) in the period 1980–2000 (*A*), 1990–2010 (*B*), 2000–2020 (*C*), and 2010–2030 (*D*). Black vertical lines represent the 2015–2017 AMJJAS rainfall anomaly (−11.5 mm/month, averaged value across GPCC, CRU, and UDEL). (*E* and *F*) Decadal probability of occurrence of a 3-y winter rainfall anomaly equal to or worse than in 2015–2017 in HIST, SSP2-4.5, and SSP5-8.5. Shading denotes the 95% CI from bootstrap resampling. The blue constant line denotes the CTRL probability for such an event, and the blue constant dashed line is from the NATURAL run after concatenating all 30 ensemble members. (*G* and *H*) Probability (risk) ratios (to the mean 1921–1980) with 95% uncertainty intervals for event_1517 in 2015–2017 (*G*) and at the end of the 21st century (2080–2100) (*H*). Models are top-down ordered from the most skillful in reproducing WRI variability and seasonal cycle (*SI Appendix*, Fig. S14 and Table S2). Asterisk (*) denotes models for which a relative threshold (first percentile) is used to estimate the probability (*Materials and Methods*). (*I* and *J*) As in *E* and *F*, but for a 4-y anomaly of the magnitude of the 2015–2017 drought.

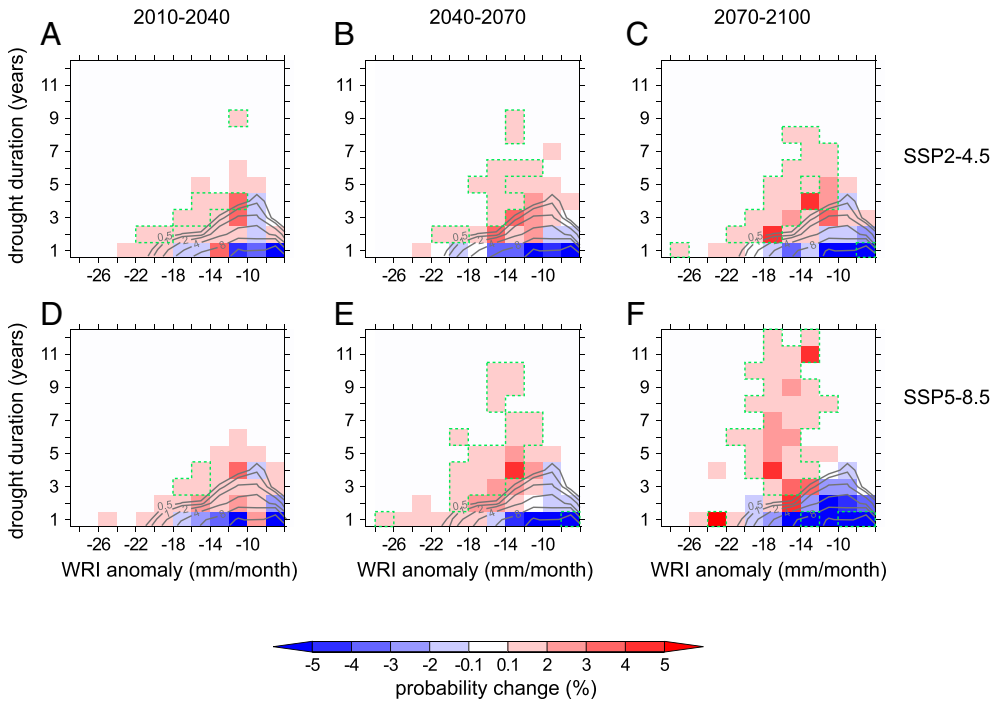

Fig. 3. (*A*–*C*) Change of probability of large annual AMJJAS rainfall anomalies ($\leq -0.75\sigma$) as a function of duration (years) and intensity (mean WRI anomaly over the drought-duration period) for the 2010–2040 period relative to 1921–1970 baseline (contours) (*A*), 2040–2070 period (*B*), and 2070–2100 (*C*) period under SSP2-4.5. The green dashed line encircles values that are outside the range of natural variability. (*D*–*F*) As in *A*–*C*, but for the SSP5-8.5 pathway.

System Model Large Ensemble (CESM-LENS) (30); and the Max Planck Institute Grand Ensemble (MPI-GE) (26) (see *Materials and Methods* and *SI Appendix* for the evaluation of these models).

All models suggest a substantial rainfall reduction (*SI Appendix*, Figs. S8*B*, S11, and S12), with CESM-LENS and MPI-GE projecting a percent precipitation reduction pretty uniform throughout AMJJAS. Mean sea-level pressure changes are overall suggestive of a poleward expansion of the descending branch of the Hadley Cell (*SI Appendix*, Fig. S10), but with anomaly patterns that are more consistent across models in AM and less consistent in June–September. Indeed, the Subtropical Anticyclone response in the Southern Hemisphere features larger intermodel uncertainty in the austral winter (40). A more prolonged dry season into the late austral fall (AM) over SSA is, therefore, a robust indication in terms of future precipitation reduction and droughts risk.

Relative to SPEAR_MED, the risk estimate is lower in SPEAR_LO (Fig. 2*G*), while FLOR suggests similar values. MPI-GE, FLOR_FA, and CEMS-LENS have a risk ratio larger than SPEAR_MED by a factor of 1.5, 1.8, and 2.8, respectively. By the end of this century, all models agree on a probability of occurrence for the event_1517 at least 90 times larger than in the 20th century (Fig. 2*H*) under the highest-emission scenarios (SSP5-8.5 or RCP8.5). Middle-of-the-road scenarios (SSP2-4.5 or RCP4.5) tend to suggest a risk ratio of about 30, while the low-emission RCP2.6 scenario (only available for MPI-GE), aiming to limit the increase of global mean temperature to 2 K, projects a risk ratio of about 13.

Conclusions

The use of a high-resolution large ensemble provides a significantly improved ability to simulate regional-scale SSA droughts in both present and future conditions, despite large internal climate variability. We find that the rainfall deficit that led to the Day Zero drought was 5.5 times more likely due to anthropogenic climate change, with a CI of [4, 8]. We therefore are able, through the use of a model with higher resolution and better climatology, to further constrain the risk ratio of SSA drought at and above the original [1.4, 6.4] estimate from ref. 5. This highlights the usefulness of high-resolution climate models to study future drought risk and provides additional guidance to design water management to avoid extreme drought.

Looking at the future, our results point to a dramatic increase in the risk of meteorological droughts of similar or even more serious magnitude by the end of the 21st century. Similarly to what occurred in 2015–2017, this increased risk of meteorological droughts is associated with a substantial rainfall reduction, especially in the shoulder season (AM and AS).

A high-emission and intermediate-emission future scenario are analyzed, highlighting that while there is uncertainty in the increase in drought risk due to future uncertainty in forcings, both scenarios lead to substantial increases, such that a drought becomes a common occurrence. Combined with the likelihood of increased water demand due to a growing population (3) and increased evaporation due to higher temperatures (41), the more frequent occurrence of wintertime meteorological droughts will likely present a major challenge for managing water resources in the region without adaptation and preparation. While these results are for SSA, such shifts in drought risk are likely to occur in other locations, with variable precipitation and large-scale circulation shifts increasing the likelihood of multiyear extreme droughts. These methods could then be applied elsewhere to identify emerging drought risks.

Materials and Methods

SPEAR Model and Experiments. The main conclusions of this study are obtained from the SPEAR (33, 42). SPEAR represents the newest modeling system for seasonal to multidecadal prediction which incorporates new model development components that have occurred in the last decade at

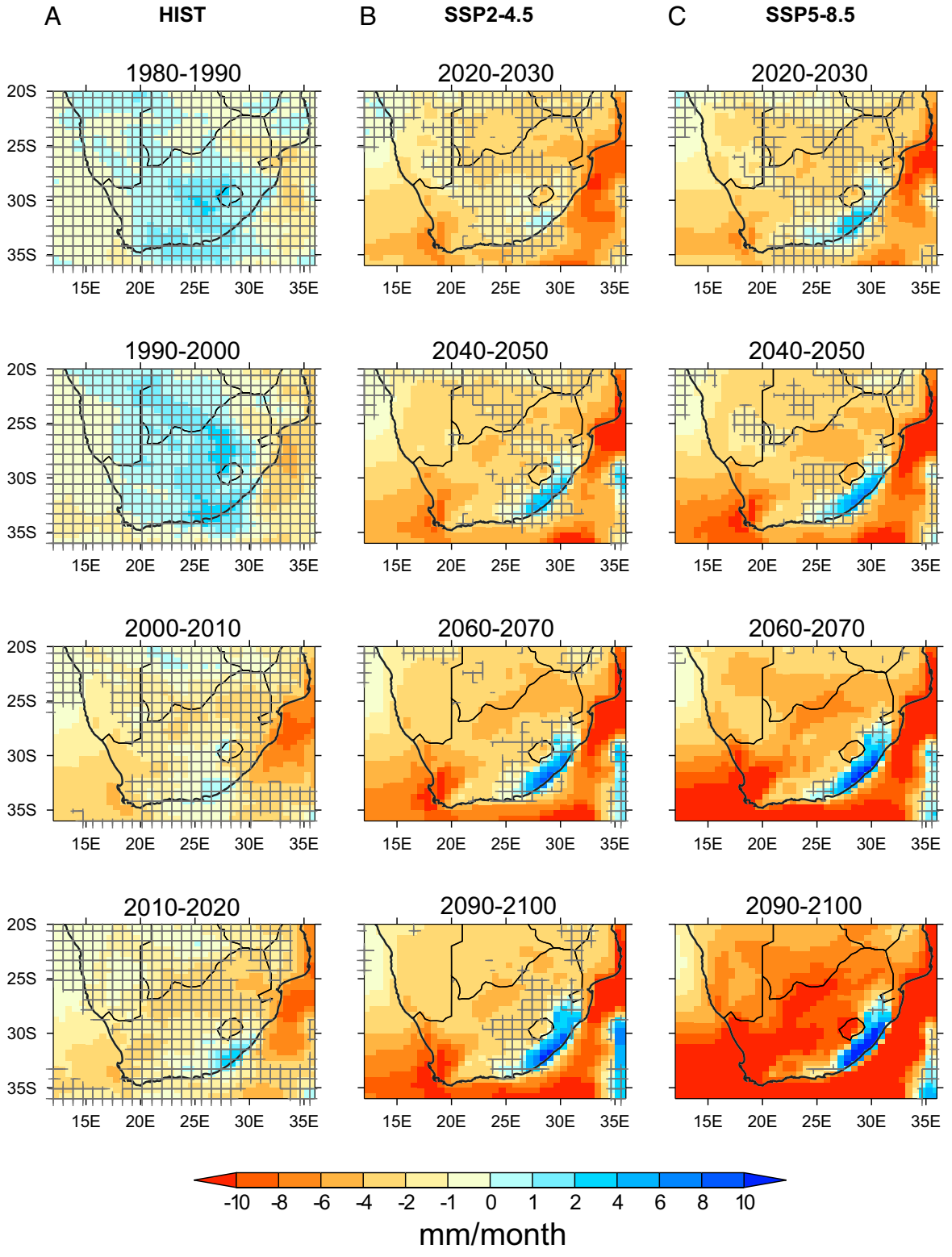

Fig. 4. Decadal evolution of wintertime (AMJJAS) rainfall mean anomalies (ensemble average, shading) relative to the 1921–1970 climate from the HIST (*A*), SSP2-4.5 (*B*), and SSP5-8.5 (*C*) runs. Gray crosses denote changes in wintertime rainfall mean state that are not distinguishable from internal climate variability, as estimated from fully coupled control simulations (see *Materials and Methods* for details).

the National Oceanic and Atmospheric Administration (NOAA) GFDL. These include: a new dynamical core (43), revised atmospheric physics (44), a new sea-ice and ocean model (45), and an enhanced land model (46). The SPEAR atmospheric model uses 33 levels in the vertical and is run at different atmospheric-land horizontal resolutions: 0.5° (SPEAR_MED) and 1° (SPEAR_LO) in this paper. The intermediate 0.5° configuration, SPEAR_MED, is a compromise between the possibility to run a large ensemble of simulations with available computation resources and retaining enough horizontal

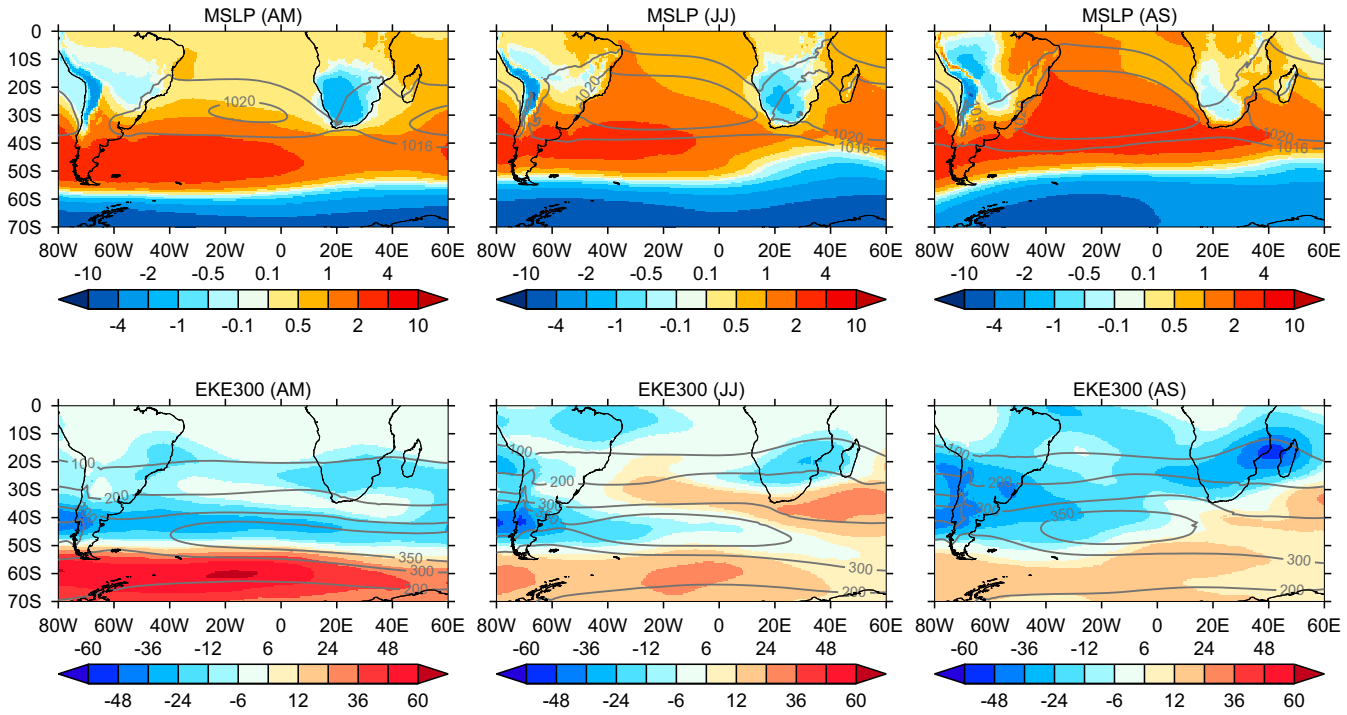

Fig. 5. Ensemble mean anomalies (shading) of AM, JJ, and AS sea-level pressure (*Upper*; hPa) and 300-hPa eddy kinetic energy (m^2 s^{-2}) for the period 2071–2100 relative to 1921–1970. Contours denote the 1921–1970 climatological values.

resolution to study regional climate and extremes. It is worth noting that the SPEAR_MED large ensemble features a horizontal grid spacing (0.5°) that is finer than those used in most of the previously used large ensembles [with the exception of FLOR (31)], thus making these GFDL ensembles a unique and unprecedented tool to study extremes and regional climate.

We used four different numerical experiments: 1) a long-term control simulation (CTRL) to evaluate unforced natural variability; 2) an ensemble driven by natural forcing only (NATURAL) to provide a baseline with only natural forcing (i.e., volcanic eruptions and solar cycles); 3) an ensemble driven by observed natural and anthropogenic forcing up to 2014 (HIST) and then according to the intermediate (≈+3 K of global warming by the end of the 21st century) SSP2-4.5 developed for the CMIP6 (35, 47); and 4) an ensemble driven by observed natural and anthropogenic forcing up to 2014 (HIST) and then according to the CMIP6 high-emission, fossil fuel-dominated (≈+5 K of global warming by the end of the 21st century) SSP5-8.5.

The 3,000-y CTRL simulation is driven by CO_2 forcing kept constant at 1850 levels. Climate drifts associated with this long-term integration are estimated to be very small and statistically insignificant for the winter SA rainfall. The 30 members of the NATURAL ensemble are driven by the same observed natural forcing (i.e., solar and volcanic) until year 2014, and by only solar forcing (quasi-11-y cycle) after 2014, with the anthropogenic forcing held fixed at the 1921 level. In the HIST + SSP5-8.5 (HIST + SSP2-4.5) ensemble, each member is driven by observed natural and anthropogenic forcing (greenhouse gases, anthropogenic aerosols, and ozone) up to year 2014 and by the SSP5-8.5 (SSP2-4.5) forcing afterward. More details about how the SPEAR large ensemble is designed can be found in Delworth et al. (2020) (33).

Model Evaluation. In addition to the model's ability to reproduce the wintertime southern African climatology (Fig. 1 *C*–*E*), the performance of SPEAR_MED in simulating wintertime rainfall variability and historical trends (1951–2017) over SSA was evaluated against three different observational land rainfall datasets: the Global Precipitation Climatology Center (GPCC) dataset (48), version 7; the Climate Research Unit high-resolution grids of monthly rainfall at the University of East Anglia (49), version 3.24; and the University of Delaware (UDEL) precipitation dataset, version 5 (http://climate.geog.udel.edu/~climate/), all at 0.5° resolution. The choice of these three gridded observed datasets, in place of scattered measurements from the South African Weather Service meteorological stations, was dictated by the need to be able to compare models with observations, as done in previous studies (5). The values of these three precipitation datasets for SSA were obtained from a limited number of stations and different interpolation algorithms. As a consequence, they can feature, locally, considerable differences (e.g., Fig. 1*A* and *SI Appendix*, Fig. S1). However, differences in area-averaged metrics like, e.g., the WRI, are minimal (Fig. 1*B*), thus making our results independent from the choice of the single precipitation dataset.

In order to have a realistic representation of the width of the distribution of rainfall anomalies, it is key that SPEAR_MED reproduces the interannual, multiannual, and decadal natural variability of the SSA winter rainfall. To check this, we worked out the SD of the detrended full, 3-y, and 10-y low-pass-filtered WRI from the three observational datasets and the SPEAR_MED ensemble members over the common period 1921–2010 (*SI Appendix*, Fig. S3). The SD of the observations was between 5 mm·$month^{-1}$ (CRU) and 6 mm·$month^{-1}$ (GPCC and UDEL) for the 3-y low-pass-filtered WRI. The SD values from the model ranged from 4 to 6.3 mm·$month^{-1}$. The observed values are, therefore, within the range from the model, suggesting that the model has the ability to properly estimate the magnitude of 3-y lasting droughts. Similarly, a good agreement between SPEAR_MED and observations exists for the SDs calculated from the unfiltered WRI time series (interannual variability) and from 10-y low-pass-filtered WRI (decadal and longer variability), too.

The effect of internal natural variability is large for SSA winter rainfall (27–29); thus, it is not appropriate to compare observed AMJJAS rainfall trends directly with the ensemble mean or with each single ensemble member, which may show contrasting signs (*SI Appendix*, Fig. S2). Instead, we evaluated if SPEAR_MED's historical trends of AMJJAS rainfall are consistent with observations over SSA. To do so, we computed rainfall trends over the last 67 y (1951–2017) in GPCC, CRU, and UDEL and compared them with individual members of the HIST + SSP5-8.5 ensembles over the same time period.

If the observed trend at one grid point was within the range of those simulated by the 30 HIST ensemble members, then we said that the model is consistent with observations in that grid box. We found that SPEAR_MED is consistent with observations over most of southern Africa (*SI Appendix*, Fig. S13).

Additional Large Ensembles. To assess the robustness and model dependence of our results, we analyzed five additional large ensembles (*SI Appendix*, Table S1): 1) the SPEAR_LO ensemble (33); 2) the GFDL FLOR model, at

0.5° land/atmosphere resolution; 3) the flux-adjusted FLOR (FLOR_FA) large ensembles, obtained imposing temperature and salinity flux adjustments at the ocean surface to FLOR (50) (both with a land-atmospheric horizontal resolution of 0.5°); 4) the CESM-LENS (30), with land-atmospheric horizontal resolution of approximately 1°; and 5) the MPI-GE (26), with land-atmospheric horizontal resolution of 1.8°. These additional large ensembles are available with various CMIP5 scenarios and are documented in *SI Appendix*, Table S1. An evaluation of the wintertime climatology over SSA showed that these models all underestimate AMJJAS mean rainfall (Fig. 1 *C–E* and *SI Appendix*, Fig. S14 and Table S2). With the exception of SPEAR_LO, these models also underestimate the SD of the full 3-y and 10-y low-pass-filtered WRI (*SI Appendix*, Fig. S3). Critically, this means that they also underestimate the width of the probability distribution of the 3-y AMJJAS rainfall anomalies (*SI Appendix*, Fig. S15). In particular, CESM-LENS and FLOR_FA have SDs that are 50% and 40% smaller, respectively, suggesting that they are poor tools for risk analysis over SSA. As they substantially underestimate the probability of occurrence of event_1517, to quantify changes in risk in a manner that implicitly accounts for model biases, we used a 3-y WRI anomaly corresponding to the first percentile, which is the percentile to which −11.5 mm/month corresponds to in observations and SPEAR_MED.

WRI. In this study, we focused on the regional-scale drought of the Western Cape. We thus used the annual time series of the WRI (29) to monitor interannual variability and monthly rainfall anomalies. To define the WRI, we first selected the grid points where at least 65% of the total annual rainfall occurred from April to September (Fig. 1 *C–E* and *SI Appendix*, Fig. S14). Then, we took the areal mean of the extended winter (i.e., April–September) rainfall over the irregular region defined above (Fig. 1 *C–E* and *SI Appendix*, Fig. S14). The WRI is, thus, the area-averaged rainfall over the portion of SSA that experiences a dry summer and a wet winter—that is, a Mediterranean rainfall regime. This area encompasses the region of intensely irrigated agriculture surrounding the metropolitan area of Cape Town, as well as the water basins of the Breede and Berg Rivers, where dams supplying water to Cape Town are located.

Detectability of the Mean Rainfall Change. To determine where and when the decadal changes in AMJJAS rainfall start being caused by external forcing, and not by multidecadal variability, we applied a Monte Carlo approach to the long CTRL run: At each grid box, we randomly chose a 10-y period and a nonoverlapping 50-y period (to mimic 1921–1970). Then, we computed the time mean difference between the 10-y and 50-y time series. This difference is solely associated with internal natural variability of the climate system. This process was repeated 30 times (to mimic the 30-member ensemble); we then took the ensemble mean of these differences. The whole process was then repeated 10,000 times to create an empirical probability distribution of these ensemble mean differences, which was used to assess the detectability of decadal changes in rainfall. Anomalies outside the range of the distribution were attributed to external forcing and considered detectable against internal climate variability (Fig. 4 and *SI Appendix*, Figs. S11 and S12).

Estimation of the Probability Distribution. We derived a probability distribution of the 3-y mean WRI anomalies due to natural variability alone from the long CTRL run. We randomly selected a 50-y and 3-y sequence (nonoverlapping) and then calculated the anomaly of the 3-y period relative to the 50-y climatology. This choice mimics the 2015–2017 mean minus the 1921–1970 mean. We repeated this process N times (N = 10,000) to form a distribution of the 3-y WRI anomalies (Fig. 2 *A–D*). The probability of occurrence of experiencing a 3-y WRI anomaly equal to or less than the 2015–2017 anomaly—as per the gridded datasets—is about 1% in CTRL and 0.7% from HIST, taking the average of decadal probabilities over 1921–1970, respectively (Fig. 2*E*). Similarly, we estimated the distribution of the 4-y WRI anomaly. The probability of occurrence of a WRI anomaly of the same intensity, but of one additional year of duration, is 0.4% and 0.2% from the CTRL and HIST, respectively.

To evaluate the decadal change in the probability of occurrence of a 3-y WRI anomaly equal to or worse than that of 2015–17, we empirically estimated a decadal-varying probability distribution using the HIST and SSP5-8.5 (SSP2-4.5) experiments. The probability distribution was estimated for a 20-y time window, so that, for example, that referred to as 2010 is built from all years from 2001 to 2020. This choice was motivated by the need to have a time period not too wide in order to assume the stationarity of the probability distribution, but, at the same time, a number of instances large enough to allow for sufficiently accurate estimates of probabilities of rare events (e.g., 100-y return time). In a 20-y time window, there are 18 different 3-y WRI anomalies (relative to the climatological reference period 1921–1970). This leads to 18 × 30 = 540 different values when considering all of the 30 ensemble members, from which we empirically built the decadal probability distribution. Once we have the decadal probability distribution, we can estimate the probability of occurrence, for each bidecadal period, of 3-y WRI anomaly equal to or less than that observed in 2015–2017 (−11.5 mm·month^{-1}, obtained averaging GPCC, CRU, and UDEL) for any random 3-y segment within the 20-y time window. The 95% CIs in these probabilities were estimated by applying bootstrap-with-replacement resampling 10,000 times. The same methodology was applied to estimate the probability of occurrence of 4-y droughts.

We quantified the uncertainty in the estimate of the decadal probability of occurrence, derived from only 540 different 3-y rainfall anomaly values, as follows: We took the long 3,000-y CTRL and randomly selected 50-y and 3-y nonoverlapping periods and estimated the difference. We repeated this step N times (with N = 10,000) to obtain a large population sample of N 3-y anomalies, from which the probability of the event_1517 was estimated to be ≈1%. From this large sample, we then randomly drew M realizations (with replacement), with $M \leq N$, and estimated the probability of occurrence. For each value of M, we repeated the last step 10,000 times and obtained 10,000 different probability estimates, which allowed us to estimate the 95% CI (*SI Appendix*, Fig. S4*B*). As expected, the CI decreased with M up to approximately [0.9%, 1.2%] for M = 10,000. For values of M less than 300, the uncertainty is so large that it is impossible to have any sensible estimate of the probability of the event. For M = 540, the CI is approximately [0.5%,1.7%], which we can consider sufficiently accurate for our purposes.

Joint Probability Distribution of Drought Intensity and Duration. The probability distribution of a drought in the Cape Town's Mediterranean area as a function of duration and intensity was estimated from the historical and projected AMJJAS WRI anomaly time series. The focus in this paper is on severe droughts; therefore, we selected, for each time series, all contiguous years for which the WRI anomaly was below −0.75 SD (≈ −6 mm·month^{-1}). With this choice, we excluded years that were moderately and very moderately dry. For each of these segments, we worked out the mean WRI anomaly by averaging the annual WRI anomaly values over the whole segment. We chose a 2-mm·month^{-1} × 1 y bin (Fig. 3) to work out the percentage of the droughts within each bin. The analysis was performed for the 1921–1970 time period and for the periods 2011–2040, 2041–2070, and 2071–2100. To evaluate if the probability differences relative to 1921–1970 are attributable to anthropogenic climate change, we applied the same method to the 3,000-y CTRL. We randomly selected a 50-y and a 30-y nonoverlapping time span and computed the number of droughts for each duration-drought intensity bin. We repeated this 30 times to mimic the 30-member ensemble and so worked out the probability differences between the 50-y and 30-y periods. The whole process was then repeated 10,000 times to create an empirical probability distribution of the probability differences for each bin: Anomalies outside the range of the distribution were attributed to external forcing and considered detectable against internal climate variability.

Data Availability. The data that support the findings of this study are deposited in the National Centers for Environmental Information at https://doi.org/10.25921/rwe5-fw03 (SPEAR, FLOR), in the Earth System Grid Federation Node at DKRZ at https://esgf-data.dkrz.de/projects/mpi-ge/ (MPI-GE) (51), and in the NCAR's Climate Data Gateway at https://doi.org/10.5065/d6j101d1 (52).

ACKNOWLEDGMENTS. We thank A. T. Wittenberg, H. Murakami, P. C. D. Milly, and two anonymous reviewers for their comments and suggestions. This report was prepared by S.P. under National Oceanic and Atmospheric Administration, U.S. Department of Commerce Award NA18OAR4320123. The statements, findings, conclusions, and recommendations are those of the author(s) and do not necessarily reflect the views of the National Oceanic and Atmospheric Administration or the U.S. Department of Commerce.

1. E. Archer, W. Landman, J. Malherbe, M. Tadross, S. Pretorius, South Africa's winter rainfall region drought: A region in transition? *Clim. Risk Manag.* **25**, 100188 (2019).

2. R. Parks, M. McLaren, R. Toum, U. Rivett, "Experiences and lessons in managing water from Cape Town" (Grantham Institute Briefing Paper 29, Grantham Institute, London, 2019).

3. P. M. Sousa, R. C. Blamey, C. J. C. Reason, A. M. Ramos, R. M. Trigo, The 'Day Zero' Cape Town drought and the poleward migration of moisture corridors. *Env. Res. Lett.* **13**, 124025 (2018).
4. N. J. Burls *et al.*, The Cape Town "Day Zero" drought and Hadley cell expansion. *NPJ Clim. Atmos. Sci.* **2**, 2–27 (2019).
5. F. E. L. Otto *et al.*, Anthropogenic influence on the drivers of the Western Cape drought 2015-2017. *Environ. Res. Lett.* **13**, 124010 (2018).
6. P. Mahlalela, R. C. Blamey, C. J. C. Reason, Mechanisms behind early winter rainfall variability in the southwestern Cape, South Africa. *Clim. Dynam.* **53**, 21–39 (2019).
7. City of Cape Town, "Water outlook 2018" (Report, Department of Water and Sanitation, Cape Town, South Africa, 2018).
8. G. Simpkins, Running dry. *Nat. Clim. Change* **8**, 369 (2018).
9. P. Wolski, How severe is Cape Town's "Day Zero" drought? *Significance* **15**, 24–27 (2018).
10. M. Muller, Cape Town's drought: Don't blame climate change. *Nature* **559**, 174–176 (2018).
11. Z. Bischoff-Mattson *et al.*, Shape of a water crisis: Practitioner perspectives on urban water scarcity and 'Day Zero' in South Africa. *Water Pol.* **22**, 193–210 (2020).
12. J. Huang *et al.*, Dryland climate change: Recent progress and challenges. *Rev. Geophys.* **55**, 719–778 (2017).
13. F. Lehner *et al.*, Projected drought risk in 1.5° C and 2° C warmer climates. *Geophys. Res. Lett.* **44**, 7419–7428 (2017).
14. B. I. Cook, J. E. Smerdon, R. Seager, S. Coats, Global warming and 21st century drying. *Clim. Dynam.* **43**, 2607–2627 (2014).
15. J. Lu, G. A. Vecchi, T. Reichler, Expansion of the Hadley cell under global warming. *Geophys. Res. Lett.* **34**, L06805 (2007).
16. D. J. Amaya, N. Siler, S. P. Xie, A. J. Miller, The interplay of internal and forced modes of Hadley cell expansion: Lessons from the global warming hiatus. *Clim. Dynam.* **51**, 305–319 (2018).
17. P. W. Staten, J. Lu, K. M. Grise, S. M. Davis, T. Birner, Re-examining tropical expansion. *Nat. Clim. Change* **8**, 768–775 (2018).
18. K. Grise *et al.*, Recent tropical expansion: Natural variability or forced response? *J. Clim.* **32**, 1551–1571 (2019).
19. P. E. Curtis, P. Ceppi, G. Zappa, Role of the mean state for the southern hemispheric jet stream response to CO_2 forcing in CMIP6 models. *Environ. Res. Lett.* **15**, 064011 (2020).
20. G. A. Meehl *et al.*, THE WCRP CMIP3 multimodel dataset: A new era in climate change research. *Bull. Amer. Meteor. Soc.* **88**, 1383–1394 (2007).
21. K. E. Taylor, R. J. Stouffer, G. A. Meehl, An overview of CMIP5 and the experiment design. *Bull. Amer. Meteor. Soc.* **93**, 485–498 (2012).
22. J. Kidston, E. P. Gerber, Intermodel variability of the poleward shift of the austral jet stream in the CMIP3 integrations linked to biases in 20th century climatology. *Geophys. Res. Lett.* **37**, L09708 (2010).
23. P. Ceppi, Y. T. Hwang, D. M. W. Frierson, D. L. Hartmann, Southern Hemisphere jet latitude biases in CMIP5 models linked to shortwave cloud forcing. *Geophys. Res. Lett.* **39**, L19708 (2015).
24. C. Li, F. Zwiers, X. Zhang, G. Li, How much information is required to well constrain local estimates of future precipitation extremes? *Earths Future* **7**, 11–24 (2019).
25. K. Van der Wiel, N. Wanders, F. M. Selten, M. F. P. Bierkens, Added value of large ensemble simulations for assessing extreme river discharge in a 2° C warmer world. *Geophys. Res. Lett.* **46**, 2093–2102 (2019).
26. N. Maher *et al.*, The Max Planck Institute Grand Ensemble: Enabling the exploration of climate system variability. *J. Adv. Model. Earth Syst.* **11**, 2050–2069 (2019).
27. N. Philippon, M. Rouault, Y. Richard, A. Favre, The influence of ENSO on winter rainfall in South Africa. *Int. J. Climatol.* **32**, 2333–2347 (2012).
28. C. Reason, M. Rouault, J. Melice, D. Jagadheesha, Interannual winter rainfall variability in SW South Africa and large scale ocean-atmosphere interactions. *Meteorol. Atmos. Phys.* **80**, 19–29 (2002).
29. B. Dieppois *et al.*, Interannual to interdecadal variability of winter and summer southern African rainfall, and their teleconnections. *J. Geophys. Res. Atmos.* **121**, 6215–6239 (2016).
30. J. E. Kay *et al.*, The Community Earth System Model (CESM) Large Ensemble Project: A community resource for studying climate change in the presence of internal climate variability. *Bull. Amer. Meteor. Soc.* **96**, 1333–1349 (2015).
31. H. Zhang, T. Delworth, Detectability of decadal anthropogenic hydroclimate changes over North America. *J. Clim.* **31**, 2579–2597 (2018).
32. C. Deser *et al.*, Insights from Earth system model initial-condition large ensembles and future prospects. *Nat. Clim. Change* **10**, 277–286 (2020).
33. T. L. Delworth *et al.*, SPEAR—The next generation GFDL modeling system for seasonal to multidecadal prediction and projection. *J. Adv. Model. Earth Syst.* **12**, e2019MS001895 (2020).
34. I. Held *et al.*, Structure and performance of GFDL's CM4.0 climate model. *J. Adv. Model. Earth Syst.* **11**, 3691–3727 (2020).
35. V. Eyring *et al.*, Overview of the Coupled Model Intercomparison Project Phase 6 (CMIP6) experimental design and organization. *Geosci. Model Dev.* **9**, 1937–1958 (2016).
36. P. Milly *et al.*, Stationarity is dead: Whither water management? *Science* **319**, 573–574 (2008).
37. D. Jakob, "Nonstationarity in extremes and engineering design" in *Extremes in a Changing Climate: Detection, Analysis and Uncertainty*, A. AghaKouchak, D. Easterling, K. Hsu, S. Schubert, S. Sorooshian, Eds. (Springer, New York, NY, 2013), pp. 363–417.
38. S. D. Polade, A. Gershunov, D. R. Cayan, M. D. Dettinger, D. W. Pierce, Precipitation in a warming world: Assessing projected hydro-climate changes in California and other Mediterranean climate regions. *Sci. Rep.* **7**, 10783 (2017).
39. M. Hauser *et al.*, Methods and model dependency of extreme event attribution: The 2015 European drought. *Earths Future* **5**, 1034–1043 (2017).
40. A. Fahad, N. J. Burls, Z. Strasberg, How will southern hemisphere subtropical anticyclones respond to global warming? Mechanisms and seasonality in CMIP5 and CMIP6 model projections. *Clim. Dynam.* **55**, 703–718 (2020).
41. P. Milly, K. Dunne, Potential evapotranspiration and continental drying. *Nat. Clim. Change* **6**, 946–949 (2016).
42. S. Pascale, W. F. Cooke, T. L. Delworth, S. B. Kapnick, Precipitation and sea level pressure model output under varying atmospheric scenarios centered over South Africa from 1921-01-01 to 2100-12-31 (NCEI Accession 0220095). NOAA National Centers for Environmental Information. https://doi.org/10.25921/rwe5-fw03. Deposited 14 October 2020.
43. L. M. Harris, S. J. Lin, A two-way nested global-regional dynamical core on the cubed-sphere grid. *Mon. Weather Rev.* **141**, 283–306 (2013).
44. M. Zhao *et al.*, The GFDL global atmosphere and land model AM4.0/LM4.0: 2. Model description, sensitivity studies, and tuning strategies. *J. Adv. Model. Earth Syst.* **10**, 735–769 (2018).
45. A. Adcroft *et al.*, The GFDL global ocean and sea ice model OM4.0: Model description and simulation features. *J. Adv. Model. Earth Syst.* **11**, 3167–3211 (2019).
46. P. Milly *et al.*, An enhanced model of land water and energy for global hydrologic and earth- system studies. *J. Hydrometeorol.* **15**, 1739–1761 (2014).
47. B. C. O'Neill *et al.*, The roads ahead: Narratives for shared socioeconomic pathways describing world futures in the 21st century . *Global Environ. Change* **42**, 169–180 (2017).
48. U. Schneider *et al.*, GPCC's new land surface precipitation climatology based on quality-controlled in situ data and its role in quantifying the global water cycle. *Theor. Appl. Climatol.* **115**, 15–40 (2013).
49. I. Harris, P. Jones, T. J. Osborn, D. H. Lister, Updated high-resolution grids of monthly climatic observations—The CRU TS3.10 Dataset. *Int. J. Climatol.* **34**, 623–642 (2013).
50. G. Vecchi *et al.*, On the seasonal forecasting of regional tropical cyclone activity. *J. Clim.* **27**, 7994–8016 (2014).
51. N. Maher, Data from "The Max Planck Institute Grand Ensemble". Earth System Grid Federation Node at Deutsches Klimarechenzentrum (DKRZ). https://esgf-data.dkrz.de/projects/mpi-ge/. Accessed 30 January 2020.
52. J. E. Kay, C. Deser, A. Phillips, Data from "The Community Earth System Model (CESM) Large Ensemble Project". National Center for Atmospheric Research's (NCAR) Climate Data Gateway. https://doi.org/10.5065/d6j101d1. Accessed 30 January 2020.